Original scientific paper

SPATIAL SPICE MODEL OF A WIRELESS SENSOR NETWORK NODE BASED ON A THERMOELECTRIC GENERATOR

Miloš Marjanović, Aleksandra Stojković, Aneta Prijić, Danijel Danković, Zoran Prijić

University of Niš, Faculty of Electronic Engieering, Niš, Serbia

Abstract. *This paper presents a spatial SPICE model of a wireless sensor network node that enables simulation of performances in the steady-state and time-domain. The model includes constructive non-electrical parts of the node and a thermoelectric generator employing the thermoelectric effects. The simulation results are compared with the experiment to validate the model. It enabled the characterization of WSN nodes comprising different thermoelectric generators and heatsinks in terms of energy conversion efficiency.*

Key words: *Spatial modeling, SPICE simulation, energy harvesting, thermoelectric generator, wireless sensor network node*

1 INTRODUCTION

Wireless sensor network (WSN) nodes are systems designed to perform telemetry functions, realized from low-power electronic devices and often self-powered. Therefore, their supply relies on the electricity obtained by converting other types of energy available from the close surrounding (solar, thermal, mechanical, electromagnetic energy). Thermoelectric generators (TEGs) are usually the core of systems that transform thermal energy into electricity. They convert the temperature difference applied on their opposite sides into electrical voltage employing the Seebeck effect. Apart from the

temperature difference, the generated voltage also depends on the material, dimensions, and construction of the TEG [1]. A WSN node with a TEG can work properly at temperature differences between the heat source/sink and the ambient of several tens of degrees. The aim is to make the WSN node of the compact, as small as possible design, with the thermal characteristics enabling efficient operation of the incorporated TEG.

Characterization of TEGs under different operating conditions and considering datasheet parameters can be realized analytically, experimentally, or by simulations. The analytical models of TEGs present a system of nonlinear differential equations solvable in the closed-form only with assumptions related to the specific thermal operating conditions [2, 3]. The experimental methods involve the extraction of thermoelectric parameters or measurement of voltage and power delivered to the load by the TEG [4, 5]. The simulations can be performed in coupled multiphysics domains based on Finite Element Modeling (FEM) [6, 7]. Also, simulations can rely on SPICE models of mutually interacting electric and equivalent thermal circuits [8–11]. Component-based models developed in the Modelica language can be used to simulate complex systems based on TEG. In [12], a transient spatial model with one-dimensional resolution for a thermoelectric module is presented, whose input parameters are material and geometric parameters. This approach avoids the electrothermal analogies introduced in SPICE models.

In this paper, a WSN node that contains a PIC microcontroller that acquires temperature values from the sensor and sends data via RF module will be used [13]. The node is realized in a compact form, using two printed circuit boards (PCBs) with an aluminum core and TEG PE-031-10-20 as a generator. This TEG contains 31 thermoelectric pairs. The aluminum core PCBs provide a more efficient temperature redistribution than PCBs made of FR-4 material [14]. Therefore, the lower PCB serves as a heat collector for the hot side of the TEG, and the upper one, in conjunction with a low-profile aluminum heatsink, enables enhanced heat dissipation to the environment. Electronic devices of the system, except the temperature sensor, are placed on the upper PCB. The space between the PCBs is filled with thermally insulating foam to reduce unwanted heat exchange. In addition to the TEG, the electronic part of the node comprises a power management and storage unit based on the LTC3108 boost circuit and a supercapacitor. The design of the node provides a reliable cold start while its overall dimensions are $(52 \times 35 \times 17.6)$mm. Experiments show that the minimum temperature difference of 15 °C between the node hot side and ambient is required for the TEG to generate a voltage of 40 mV at which the boost circuit begins to

provide sufficient voltage for system operation. In this case, the cold start time is 90 s. At a temperature difference of 25 °C, the cold start time is 20 s with 2.04 mW of the collected power. The Computer-Aided Design (CAD) model of the described WSN node enables carrying out appropriate FEM electro-thermal steady-state [6] and SPICE time-dependent [15] simulations of its operation.

The FEM simulations performed in the multiphysics domain (mechanical, thermal, and electrical) are the most accurate in assessing the performance of systems like WSN nodes. However, such simulation tools are poorly compatible with simulators used in electrical circuit design. Therefore, the SPICE simulations represent an efficient approach in designing and optimizing WSN nodes to select the appropriate TEG from several aspects (efficiency, minimum operating temperature, node dimensions). In that manner, there is a need to develop equivalent spatial (3D) SPICE models of non-electrical parts of the system to achieve satisfying simulation accuracy. The heat transfer analogy using RC circuits, according to our literature research, was first introduced in 1965 [16]. This well-known method was used to model the thermal effects of various electronic devices [4, 9, 17, 18]. Also, the concept of the spatial RC model was first introduced in 1999 for modeling interconnections in integrated circuits [19]. This concept was later used by other authors to model hybrid synchronous machines [20], interconnections for the reliability analysis [21], solar cells [22]. In [23], the authors described a general equivalent model for temperature distribution that takes into account lateral and vertical heat flow and temperature absorption. The model includes thermal resistances and capacitances, as well as a current generator that simulates the flow of heat originating from the power generated in the building cell. The authors presented the concept of connecting several elementary cells with the aim of electrothermal simulation of complex systems. The authors of [24] proposed a compact thermal model that can be used in the process of designing integrated circuits with liquid cooling, realized in MEMS technology. The spatial model of the solid parts of the system is based on the thermal RC network, while for the modeling of the liquid cooling subsystem the model is extended by voltage controlled current sources representing the heat flow in/from the microchannel. The model was successfully verified by comparison with experimental data, on the example of a 3D multiprocessor system on a liquid-cooled chip. The system is described in the simulation by the interconnection of elementary cells. The concept of a spatial thermal model with distributed thermal resistances within an elementary cell was used in [21]. The authors used this modeling

approach to demonstrate an improved extended Kryl subspace method to increase the simulation speed of VLSI circuits with a large number of input ports. They showed that by applying this method, the simulation time is independent of the number of input ports. In the paper [25], the RC spatial network of the chip was used for thermal analysis. The authors compared the simulation time of this modeling approach for two iterative methods, such as Cholesky Preconditioned Conjugate Gradient (ICCG) and the proposed Fast Transform Preconditioned Conjugate Gradient Fast Transform Preconditioned (FT-PCG). Thermoelectric effects were introduced into the spatial model for the first time in [26]. The authors successfully applied a model for simulating thermoelectric harvesters on a chip. This paper was the starting point for modeling our WSN node. Unlike the original model [26], in this paper the thermal and electrical resistances are modeled with parametrically defined resistors, without the use of dummy resistances, thus reducing the number of elements in the equivalent circuit. One of the most recent studies using a spatial equivalent RC model was published in [27]. The authors modeled a thermoelectric system consisting of a Peltier element and a metal plate in the Simscape-Simulink process control simulation environment. The spatial model has been successfully applied to describe the transfer of heat by conduction and convection through a metal plate. The advantage of this kind of model is that its parameters can be determined without additional experiments. Dimensions can be taken from the datasheet of thermoelectric modules, while material parameters can be used from relevant databases [28, 29]. The disadvantage of the spatial model is the complex equivalent circuit, but it does not cause convergence problems in the transient simulation.

This paper presents a spatial SPICE compatible model of a wireless sensor network node that contains non-electrical parts (such as aluminum PCBs and heatsink) and a TEG, based on the model proposed in [26]. The model of TEG, in addition to heat transfer through its ceramic plates, includes the thermoelectric effects that occur within the device. The model enables the electric and thermal characterization of WSN nodes with different TEGs and heatsinks. Moving beyond conventional FEM solvers, this paper presents an approach for rapid electrical simulation of complex electromechanical systems, such as the WSN node: offers faster solution and uses less memory than FEM solvers. This overcomes the computational demands for very large systems.

2   SPATIAL SPICE COMPATIBLE MODEL

2.1   Modeling of non-electrical parts of the WSN node

The WSN node described in this paper has several non-electrical parts that determine the system performance by their thermal properties - aluminum PCBs, aluminum stand, thermal glue layers, thermal insulation foam, TEG ceramic plates, and a heatsink. The spatial equivalent SPICE model of each part, based on an electrothermal analogy (Table 1), can be represented by appropriate electrical quantities. This is a well-known approach to modeling, which has been used for more than 20 years [19, 21, 23, 24, 26]. The building cell of the model has dimensions x, y, z, as shown in Fig. 1. Each cell is characterized by the absolute temperature at the central point T and temperatures at its surfaces T_{ij} $(i = x, y, z; j = 1, 2)$. The total thermal resistance of the cell is distributed along the coordinate axes from the central point to each surface. Partial thermal resistances are:

$$R_{thx} = \frac{1}{2\lambda}\frac{x}{yz}, R_{thy} = \frac{1}{2\lambda}\frac{y}{xz}, R_{thz} = \frac{1}{2\lambda}\frac{z}{xy}, \tag{1}$$

where λ is the thermal conductivity of the material. This value is temperature-dependent, with the value of λ_0 at the reference temperature $T_{ref} = 300\,\mathrm{K}$ and the temperature coefficient a_λ. Therefore, thermal resistances are modeled by parametrically dependent resistors according to the following:

$$R_{thi} = \frac{R_{thi0}}{1 + a_\lambda(T - T_{ref})}, (i = x, y, z). \tag{2}$$
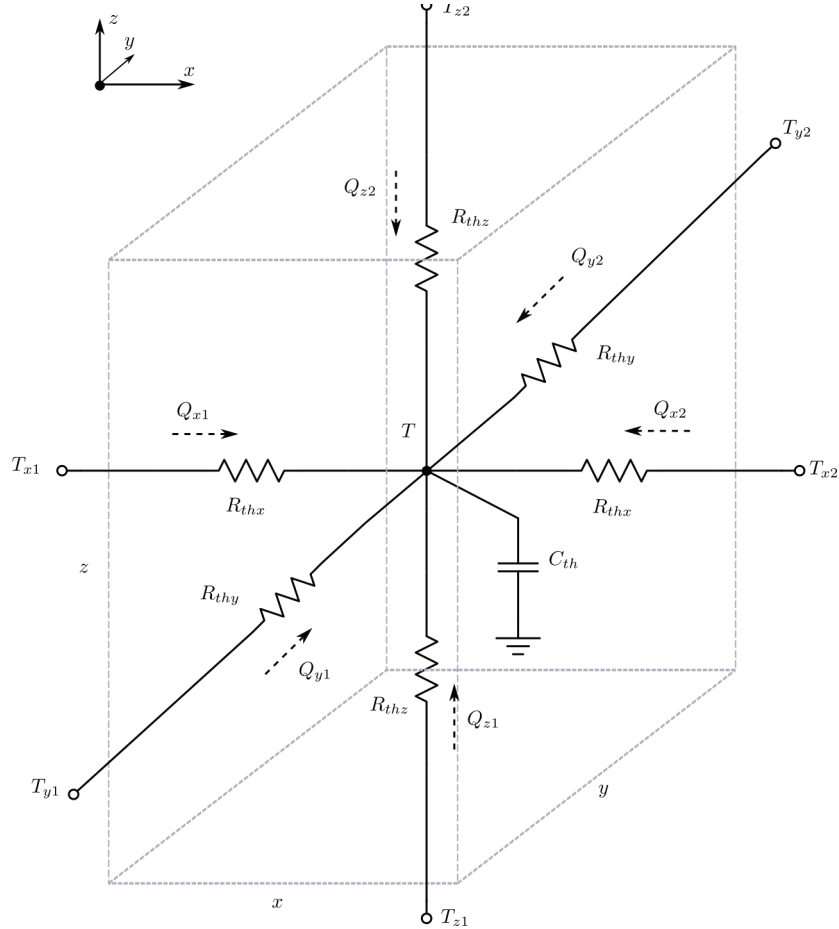
Fig. 1: The building cell of the SPICE compatible spatial equivalent model of the non-electrical WSN node parts. Based on [19, 21, 24].

The total cell thermal capacitance C_{th} is connected between the central point of the cell and the thermal ground ($0\,\mathrm{K}$). The value of thermal capacitance is:

$$C_{th} = c_p d V_{cell}, \tag{3}$$

where c_p is the specific heat capacity of a material, d is the density of the material, and $V_{cell} = x \times y \times z$ is the volume of the building cell.

The heat flow from the cell surface toward the center (Q_{ij}) follows the Fourier law of heat conduction:

$$T_{ij} - T = R_{thi} Q_{ij}, (i = x, y, z,); (j = 1, 2). \tag{4}$$

The temperature in the central point of the building cell is set as an initial condition and usually equals the ambient temperature.

Table 1: The analogy between electrical and thermal quantities [17, 18, 30].

Electrical quantity	Thermal quantity
Voltage $V(\mathrm{V})$	Temperature $T(\mathrm{K})$
Current $I(\mathrm{A})$	Heat flux $Q(\mathrm{W})$
Resistance $R(\Omega)$	Thermal resistance $R_{th}(\mathrm{K\,W^{-1}})$
Capacitance $C(\mathrm{F})$	Thermal capacitance $C_{th}(\mathrm{J\,K^{-1}})$

2.2 Modeling of thermoelectric generator

The thermoelectric generator consists of the number of thermoelectric pairs electrically connected in series via metal contacts and thermally in parallel via two ceramic plates. TEG ceramic plates are non-electrical parts, and they are modeled adequately. On the other hand, the thermoelectric pairs consist of legs made of semiconducting n and p-type doped Bi-Te or Pb-Te alloys, and the TEG model should include thermoelectric effects. The inspiration for this model came from the original model shown in [26] used to simulate a thermoelectric module on a chip. In this paper, the original model is simplified and applied for simulation of a thermoelectric generator, as an integral part of a WSN node. Fig. 2 shows the schematic of the SPICE compatible spatial model of the one thermoelectric leg representing the building cell. Mobile charge carriers inside the thermoelectric leg diffuse from the hot side toward the cold side when exposed to the temperature difference. The accumulation of charge carriers results in a net charge (negative for electrons and positive for holes) on the cold side of the leg and the appearance of voltage. The connections between the quantities related to one thermoelectric leg as a building cell are as follows. The electric potential v_{i1} will appear on one side of the cell due to the temperature T_{i1}, and the potential v_{i2} will appear on the other side of the cell due to temperature T_{i2}:

$$v_{i1} = \alpha T_{i1}, \tag{5}$$
$$v_{i2} = \alpha T_{i2}, (i = x, y, z). \tag{6}$$

Here, α is the Seebeck coefficient of thermoelectric material (n- or p-type semiconductor) which is temperature-dependent. It has value α_0 at the reference temperature $T_{ref} = 300\,\mathrm{K}$ and the temperature coefficient a_α. Therefore, the electrical part of the SPICE model in Fig. 2 contains two behavioral

voltage generators (designated as V_{i1} and V_{i2}) whose values equal the potentials v_{i1} and v_{i2} [26]. The value of the voltage across the cell along a certain axis in the open circuit mode represents Seebeck voltage:

$$V_i = v_{i1} - v_{i2} = \alpha_0[1 + a_\alpha(T - T_{ref})](T_{i1} - T_{i2}), (i = x, y, z). \qquad (7)$$

The difference of temperatures T_{i1} and T_{i2} determines the sign of the generated voltage.

The electrical resistance of the thermoelectric leg of a defined type of semiconductor represents part of the TEG internal resistance R_{TEG}. The electrical resistance of the building cell is distributed along the coordinate axes from the central point to each surface. These partial electrical resistances are:

$$R_x = \rho\frac{x}{2yz}, R_y = \rho\frac{y}{2xz}, R_z = \rho\frac{z}{2xy}, \qquad (8)$$

where ρ is the electrical resistivity of the thermoelectric material, which is temperature-dependent with the temperature coefficient a_ρ. In the SPICE model, the resistances are modeled by a parametrically dependent resistors according to the expression:

$$R_i = R_{i0}[1 + a_\rho(T - T_{ref})], (i = x, y, z), \qquad (9)$$

where R_{i0} is partial electrical resistance at the reference temperature.

The load R_L connected to the TEG closes an electrical circuit and enables the flow of electrical current I_L. This current flows through thermoelectric legs and has components - i_{ij}. It leads to the appearance of Peltier and Joule effects. The Peltier effect causes heat absorption on one surface of the leg and heat release on the other surface:

$$Q_{Pelt_{ij}} = \alpha_0[1 + a_\alpha(T - T_{ref})]T_{ij}i_{ij}, (i = x, y, z); (j = 1, 2). \qquad (10)$$

The thermal part of the SPICE model needs to be expanded to incorporate these, and six arbitrary behavioral current generators are added. Their values represent the product of the voltage across the generators V_{ij} and the current through them [26] (see Fig. 2):

$$Q_{Pelt_{ij}} = (v_{ijj} - v_{ij})i_{ij}, (i = x, y, z); (j = 1, 2). \qquad (11)$$

The Joule effect also governs the operation of the TEG. It manifests as heat dissipated by material with non-zero electrical resistance in the presence of an electrical current. The heat generated by each component of the cell electrical resistance is:

$$Q_{Joul_{ij}} = (v_{ijj} - v_0)i_{ij}, (i = x, y, z); (j = 1, 2). \qquad (12)$$

The SPICE model for the Joule effect contains six arbitrary behavioral current generators, one for each resistance [26]. Since all generators source the current to the central point of the cell, their sum is presented with only one generator in Fig. 2.

The thermoelectric pair consists of thermoelectric legs with Seebeck coefficients of the opposite signs, and voltages produced by each are added together. Overall, the TEG with N thermoelectric pairs exposed to temperature difference ΔT^* (on the hot side of the structure is T_{hot} and on the cold side is T_{cold}) generates a Seebeck voltage:

$$V_{TEG} = N\alpha_{n,p}(T_{hot} - T_{cold}) = N\alpha_{n,p}\Delta T^*. \tag{13}$$

The overall Seebeck coefficient for n- and p-type semiconductors $\alpha_{n,p} = \alpha_p - \alpha_n$ is also temperature-dependent. The flow of the electrical current causes voltage drop on the internal TEG resistance, and voltage on the load is:

$$V_L = V_{TEG} - R_{TEG}I_L = R_L I_L. \tag{14}$$

2.3   Complete WSN node model build-up

The LTSpice program [31] was used for simulations. The simulation methodology (Fig. 3) involves three main steps. The first is the definition of SPICE netlist for a building cell, in the form of the subcircuit, based on the models described in Subsections 2.1 and 2.2. The next step is forming the building cell symbol with appropriate nodes and its assignment to a SPICE netlist. The final step includes creating the main simulation file describing all system parts using the building cells and setting the simulation conditions. The building cells of non-electrical parts (aluminum PCBs, stand, heatsink, TEG ceramic plates, thermal glue layers, thermal insulation foam) have a total of 6 nodes (T_{x1}, T_{x2}, T_{y1}, T_{y2}, T_{z1}, T_{z2}). The building cells of thermoelectric legs of n- and p- type have additional 6 nodes (v_{x1}, v_{x2}, v_{y1}, v_{y2}, v_{z1}, v_{z2}). The model allows steady-state and transient simulations.

3   EXPERIMENTAL SETUP

The experiments were conducted in the laboratory using the setup illustrated in Fig. 4. This setup enables controlled heat flux input and measurement of relevant temperature and voltage values in the time domain. A thermoelectric module (TEM) serves as a heat source - heater. The programmable

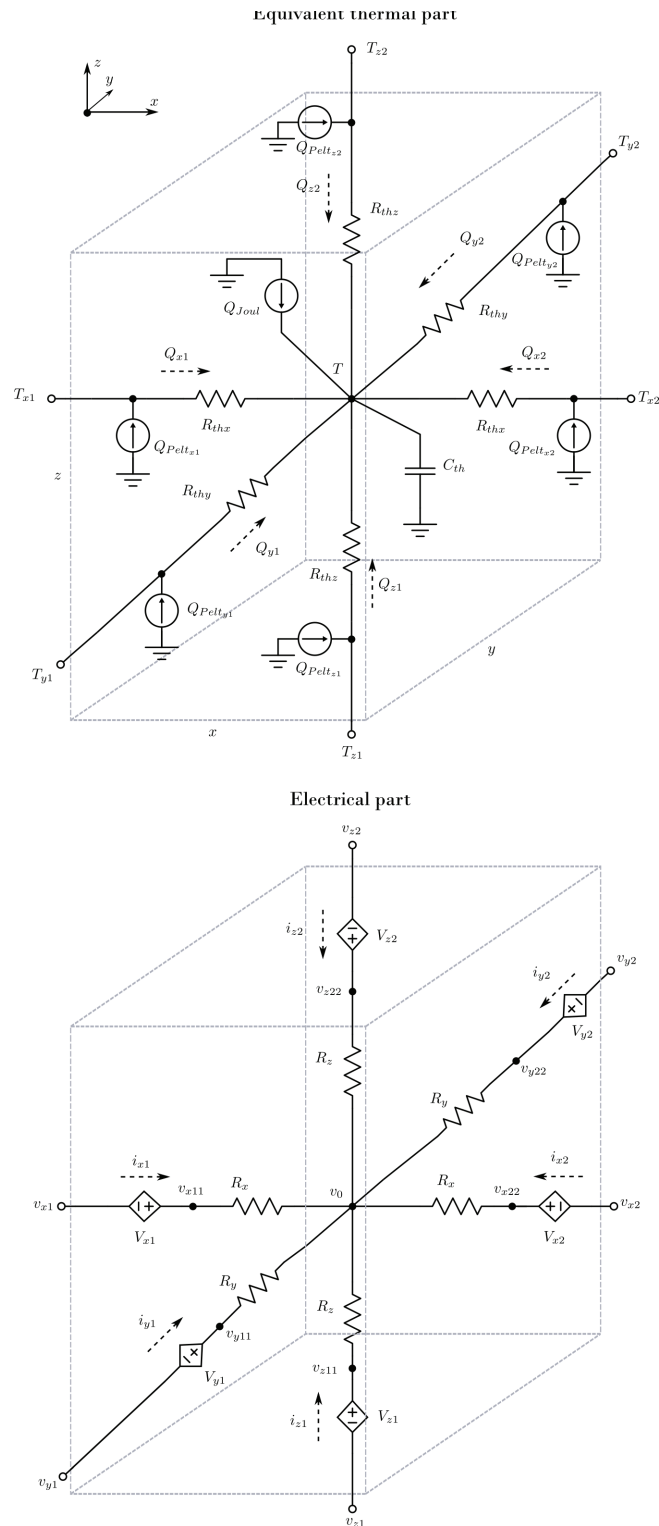**Equivalent thermal part**

Electrical part

Fig. 2: The SPICE compatible spatial equivalent model of the thermoelectric leg as a building cell. Based on [26].
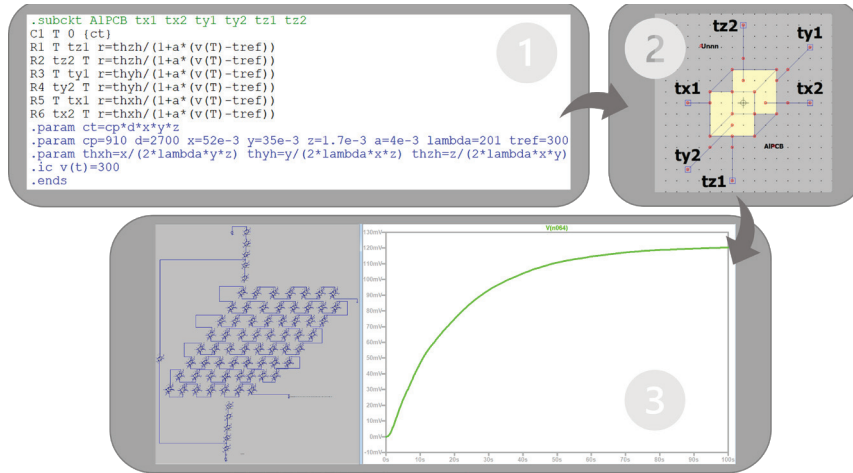
Fig. 3: Block diagram of the simulation methodology.

laboratory DC power supply powers TEM with a current in the range of 0.5-2A. A large aluminum heatsink dissipates heat from the cold side of the TEM. The experimental setup fulfills the conditions of natural convection heat dissipation where a device under test (DUT) stands on the heater horizontally as the worst-case design. Thermally conductive glue establishes good thermal joints between the heater and DUT. Two thermocouples connected to a digital thermometer measure temperatures of the ambient T_{AMB} and heater T_{HEAT}.

Experimental characterization was done for the assembly consisting of TEG ET-031-10-20 by Adaptive and flared fin low profile aluminum heatsink of dimensions (35 × 35 × 7.5) mm as DUT1 and described compact WSN node as DUT2. In the experiment, DUT at temperature T_{AMB} is instantaneously placed on a heater of the defined temperature T_{HEAT}. The oscilloscope records the value of the voltage delivered to the load by the DUT. Three values of the temperature difference $\Delta T = T_{HEAT} - T_{AMB}$ were preset for DUT1 and one value for DUT2.

4   Results and Discussion

The simulations consider three different TEGs whose geometric, electrical, and thermal parameters are presented in Tables 2 and 3. TEGs differ by the number of thermoelectric pairs and dimensions of thermoelectric legs and ceramic plates. The selection of TEGs considers their internal resis-
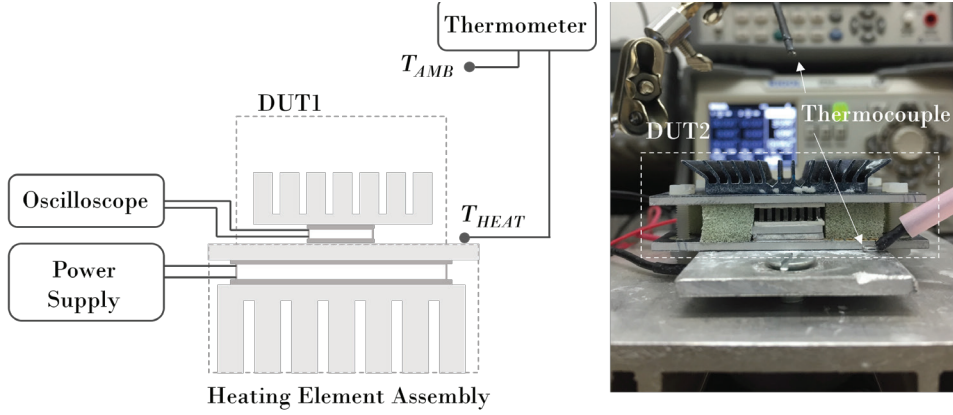
Fig. 4: Block diagram and photograph of the experimental setup.

tances that need to be close to the input resistance of the load (LTC3108 circuit) to achieve the maximum power transfer. Performances of the WSN node considerably depend on the mounted heatsink, and three of them with distinct geometries and made of different materials were considered in the simulations. Table 4 presents geometric and thermal parameters of the selected heatsinks, and Table 5 shows these parameters for other non-electric parts of the WSN node. Note that the dimensions of non-electric parts are for the WSN node used in the experiments, while in simulations with other selected TEGs, these dimensions are scaled according to the dimensions of the TEG.

Table 2: Geometric properties of the considered TEGs.

Manufacturer Part No. → Parameter	ET– 031-10-20 (TEG1) [32]	ET– 071-08-15 (TEG2) [33]	GM200– 71-14-16 (TEG3) [34]
Number of thermoelectric pairs N	31	71	71
External dimensions $L \times W \times H$ (mm)	15×15×4.3	18×18×3.8	30×30×3.8
Thermoelectric leg dimensions $w \times w \times l$ (mm)	1×1×2	0.8×0.8×1.5	1.4×1.4×1.6
Ceramic plate thickness l_P (mm)	0.75	0.75	0.8

Table 3: Thermal and electrical properties of the considered TEGs. Collected from: [11, 35–37]

Parameter	Value
p-leg Seebeck coefficient at T_{ref} - α_{p0} (μV K^{-1})	198
n-leg Seebeck coefficient at T_{ref} - α_{n0} (μV K^{-1})	-198
Temperature coefficient of α_p and α_n - a_α (K^{-1})	$2 \cdot 10^{-3}$
Thermoelectric leg thermal conductivity at T_{ref} λ_0 (W m^{-1} K^{-1})	1.5
Temperature coefficient of λ - a_λ (K^{-1})	$-2.2 \cdot 10^{-3}$
Ceramic plate thermal conductivity at T_{ref} λ_{P0} (W m^{-1} K^{-1})	25
Temperature coefficient of λ_{P0} - a_{λ_P} (K^{-1})	$-2.7 \cdot 10^{-3}$
Electrical resistivity of the thermoelectric leg at T_{ref} ρ_0 ($\mu\Omega$ m)	11.4
Temperature coefficient of ρ - a_ρ (K^{-1})	$3.4 \cdot 10^{-3}$
Thermoelectric leg density - d_{TEG} (g cm^{-3})	7.74
Ceramic plate density - d_P (g cm^{-3})	3.57
Thermoelectric leg specific heat capacity c_{TEG} (J g^{-1} K^{-1})	0.165
Ceramic plate specific heat capacity - c_P (J g^{-1} K^{-1})	0.837

Simulation of the assembly TEG1 - HS1 (DUT1 in the experiments) enabled the validation of the developed SPICE model. Fig. 5 shows a simplified simulation schematic of this assembly. Every non-electrical assembly part (two thermal glue layers, two ceramic plates, and a heatsink) has its own building cell in the schematic. Also, each of 62 thermoelectric legs is represented by one building cell, while only 6 of them are shown for clarity. Metal contacts that connect thermoelectric legs in series are very thin and have very high electric conductivity. Therefore, they are represented by simple electrical wires. The resistor $R_L = 1\,\text{M}\Omega$ simulates an open circuit condition when $V_L = V_{TEG}$. The top node of the lower ceramic plate is connected to the nodes at the bottom of each thermoelectric leg (label h). Similarly, the top nodes of the thermoelectric legs are connected to the bottom node of the upper TEG ceramic plate (label c). Note that the heatsink to ambient thermal resistance (R_{SA}) was taken into account within the heatsink building cell, as explained in [41]. The voltage generators T_{HEAT} and T_{AMB} are analog to the temperatures of the heat source and the environment, respectively. The resistor $R_{HEAT} = 0.4\,\text{K W}^{-1}$ represents

Table 4: Properties of the considered heatsinks [38–40].

Parameter	HS1	HS2	HS3
Material	Aluminum	Alumina	Microporous ceramics
Geometry	14 Flared Fins	121 Pin Fins	Flat
External dimensions $L \times W \times H$ (mm)	35×35×7.5	42×42×12	40×40×2.5
Heatsink to ambient thermal resistance - R_{SA} (K W^{-1})	8	9.4	9.7
Density - d (kg m^{-3})	2700	3660	1800
Specific heat capacity - c_p (J kg^{-1} K^{-1})	910	880	670
Thermal conductivity at T_{ref} - λ_0 (W m^{-1} K^{-1})	201	25	125
Temperature coefficient of λ - a_λ (K^{-1})	$4 \cdot 10^{-3}$	$-2.7 \cdot 10^{-3}$	0

the thermal resistance of the heat source.

The results of the simulation and experiment are shown in Fig 6. After reaching the initial peak value, the generated voltage decreases slowly due to the slow charging of the large heatsink thermal capacitance and the small area through which the heat is transferred from the TEG. The peak values of the V_{TEG} are from 175 mV at $\Delta T = 15$ °C up to 275 mV at $\Delta T = 25$ °C. Experimental and simulation results show the same tendency with the maximum difference of 12.5%, confirming the model validity. In our previous research [15], it was also shown that a simple RC equivalent model of a WSN node gives similar results in terms of deviation between simulation and experiment.

Fig. 7 shows the simulation schematic of the WSN node. Each non-electrical part is represented by a separate building cell. For clarity, only two thermoelectric legs of the TEG (one thermoelectric pair) are shown, along with their principal electrical connection. The basic schematic follows the path of heat transfer, from the heat source (T_{HEAT}) through all parts of the node to the ambient (T_{AMB}). Again, the R_{SA} thermal resistance is within the heatsink building cell, and the R_{HEAT} value is 0.4 K W^{-1}. The building cell of the thermal insulation foam is connected in the feedback loop between the top of the lower PCB and the bottom of the upper PCB because

Table 5: Properties of the non–electrical WSN node parts [29]

Parameter	Al PCB	Thermal glue	Insulating Foam	Al Stand
External dimensions $L \times W \times H$ (mm)	52×35×1.7	15×15×0.2 35×35×0.2	52×35×13.8	15 ×15×1.6
Density d (kg m^{-3})	2700	2440	1580	2700
Specific heat capacity c_p (J kg^{-1} K^{-1})	910	2090	820	910
Thermal conductivity at T_{ref} λ_0 (W m^{-1} K^{-1})	201	1.1	0.4	201
Temperature coefficient of λ - a_λ (K^{-1})	$4 \cdot 10^{-3}$	0	0	$4 \cdot 10^{-3}$

it represents a thermally high resistive element on the path of the heat flow between these PCBs. The resistor R_L is the electrical load of the TEG, and its value represents the input resistance of the LTC3108 boost circuit when it charges the primary and backup capacitors and depends on the I_L current value. The dependence of R_L on I_L is given in Table 6. Although the LTC3108 circuit has its own SPICE model, due to its complexity, it considerably extends the simulation time, demands precise initial conditions and causes convergence issues. This is the reason that it is included as a behavioral resistor in the simulation, with values defined by a lookup table with linear interpolation.

Table 6: Dependence of the WSN node load resistance on the load current [42].

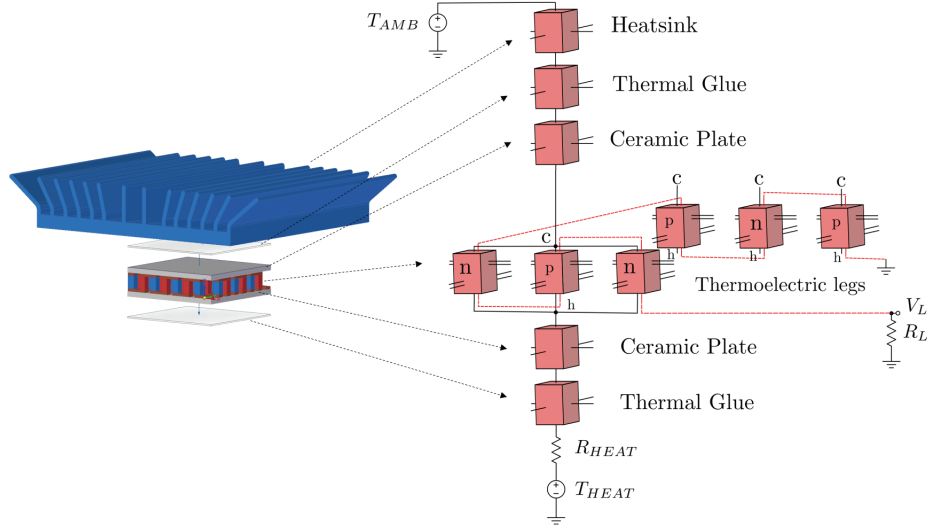| I_L (mA)	0	3	5	7.3	9	10	13	20	26	30	79	100	200
R_L (Ω)	10	7	5	4.1	4	3.9	3.8	3	2.7	2.7	2.5	2.5	2.5

Fig. 5: Simulation schematic for TEG1 - HS1 assembly; For clarity, only 6 of 62 thermoelectric legs are shown, with their electrical connection marked in red.

The results of the experimental measurement and simulation of the WSN node are shown in Fig 8. It presents the variation in time of the load voltage delivered by the TEG to the LTC3108 boost circuit (V_L), and the voltage that this circuit produces to supply other electronic devices of the WSN node (V_{OUT}) at a temperature difference of $\Delta T = 25\,°C$. The load voltage increases slowly and reaches a constant value after several tens of seconds. After $50\,s$, its value is $100\,mV$. The thermal response of the node is governed by the thermal coupling between WSN node building elements, characterized by the time needed to charge their thermal capacitances. The heat transfer goes from the heater to the bottom PCB and afterward to the rest of the node, mainly through the aluminum stand and TEG. Heat transfer through the thermal foam is minimal due to its high thermal resistance. The top PCB acts as an extension of the heatsink base and enhances overall heat dissipation. Experimentally measured voltages have the drops at the time instances when the WSN node transmits data (Fig. 8b). These oscillations translate to the input of the LTC3108 converter due to its generic operation principle. This effect is not included in the model. However, the simulation results follow the load voltage tendency during the overall WSN node operation interval.

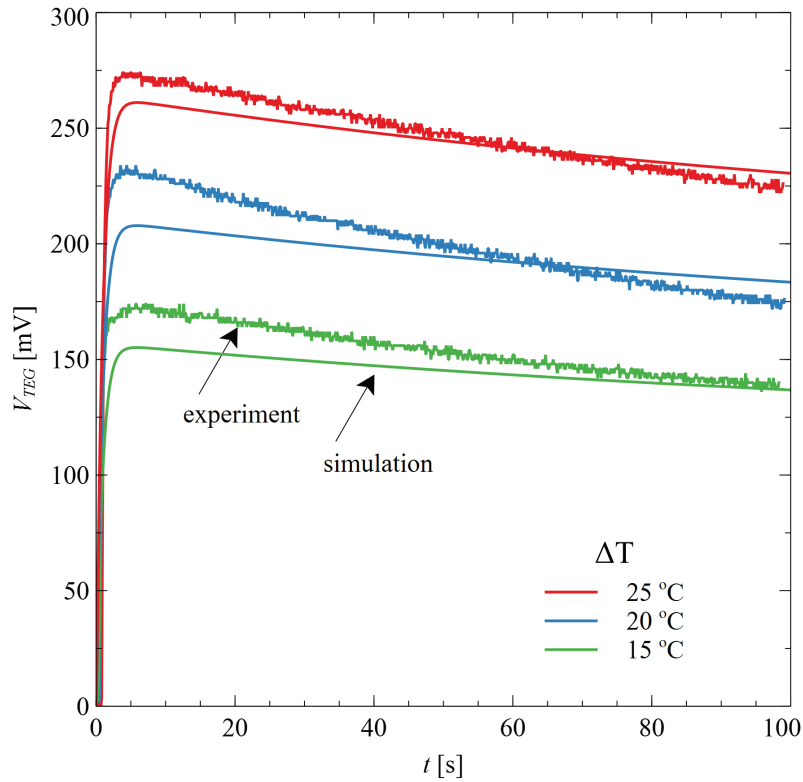The model was used to characterize WSN nodes with different TEGs and

Fig. 6: Generated voltage vs. time for the TEG1-HS1 assembly at three temperature differences.

heatsinks, whose characteristics summarize Tables 2 and 4, respectively. The combinations of each TEG with each heatsink give nine configurations to investigate. Dimensions of other parts of the WSN node are scaled according to the dimensions of the selected TEG and heatsink. The simulation results give the V_L values in steady-state as a function of temperature difference (ΔT) for all node configurations, as shown in Fig 9. The range of considered temperatures is a common one necessary for the successful start-up of self-powered systems containing the LTC3108 converter. The value of V_L increases linearly with increasing temperature differences. TEG3 generates the highest voltage values for all heatsinks compared to the other two TEGs, which is most observable at the higher temperature differences. At a temperature difference of 25 °C, TEG3 generates a voltage of 200 mV, which is 72 % higher than TEG1 and 40 % higher than TEG2. The WSN node with TEG1 will reach the voltage of 100 mV at the temperature difference of
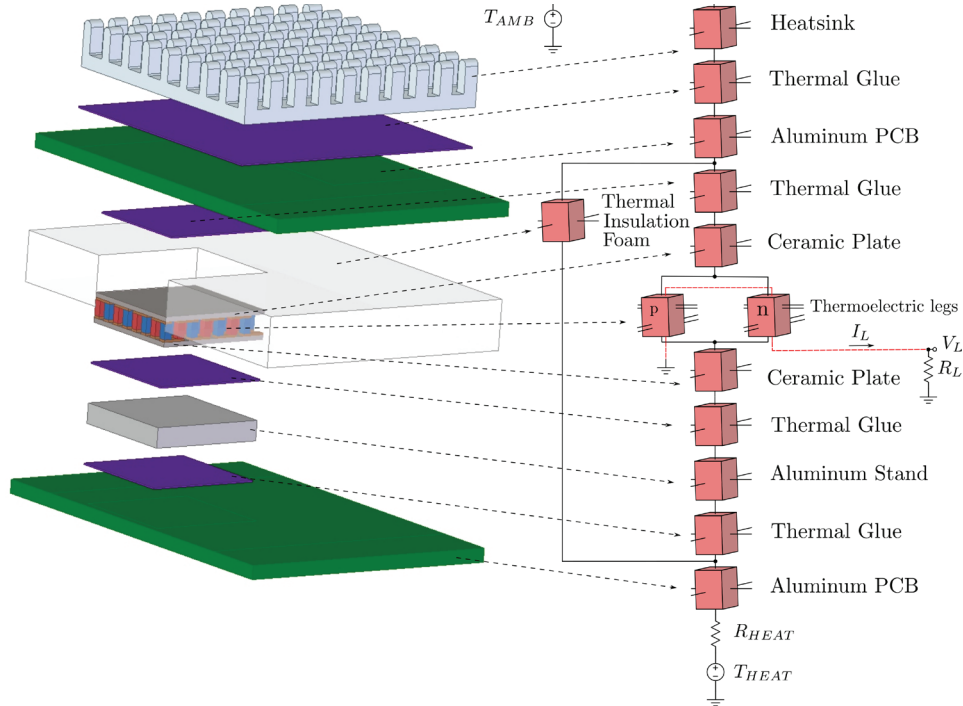
Fig. 7: Simulation schematic for WSN node; For clarity, only 2 of 62 thermo-electric legs are shown, with their electrical connection marked in red.

25 °C, while the same voltage for the node with TEG2 will be at $\Delta T = 20$ °C, and with TEG3 already at $\Delta T = 15$ °C. The reason for all this is the larger number of thermoelectric pairs in the TEG, i.e., its larger surface area. Although TEG2 and TEG3 have the same number of thermoelectric pairs, the greater length and cross-section area of the thermoelectric legs cause TEG3 to generate a higher voltage than TEG2. On the other hand, due to their volumes, TEG3 will increase the overall dimensions of the WSN node by 37 % and TEG2 by 6 %. Since TEG1 has smaller dimensions than the other two TEGs, it is acceptable for applications where miniaturization of the WSN node is of primary importance, despite requiring larger temperature differences to achieve the minimal load voltage value.

The choice of heatsinks affects the value of the generated load voltage. Heatsinks made of aluminum (HS1) and alumina ceramics (HS2) show superior characteristics compared to the heatsink made of microporous ceramics (HS3) because they have a large number of fins and a large free surface area, but also greater overall volume. On the other hand, HS3 has a simple ge-
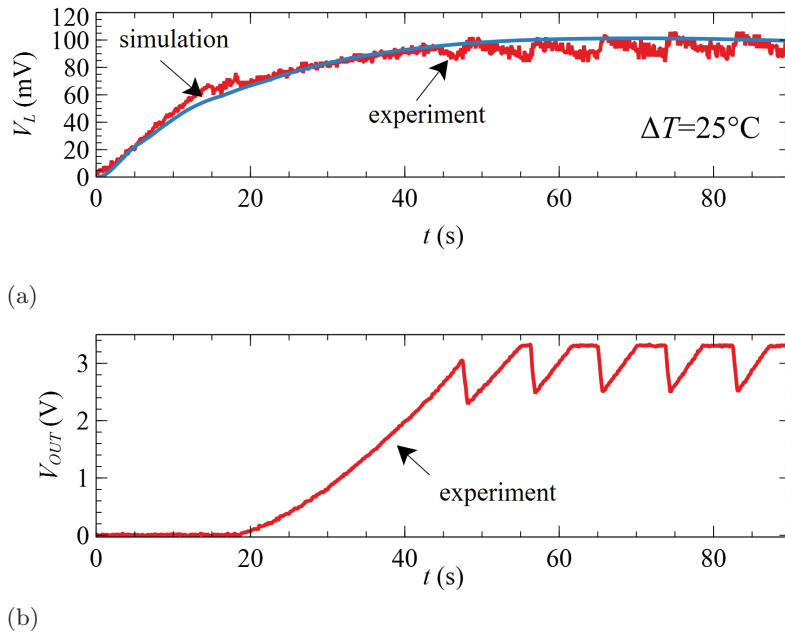
Fig. 8: Voltages in the WSN node for $\Delta T = T_{HEAT} - T_{AMB} = 25\,°C$: (**a**) Load voltage vs. time; (**b**) Supply voltage vs. time.

ometry of low height which contributes to minimizing the overall dimensions of the WSN node. WSN node with TEG3 at $\Delta T = 25\,°C$ will generate a voltage of 158 mV with HS1, while with HS2 this voltage will be 28 % higher, and with HS3 30 % lower. The performance of the WSN node with TEG1 and HS2 is the same as the performance of the node with TEG2 and HS1. Quantitative analysis of all combinations shows that the heatsink of alumina ceramic produces about 30 % higher and the microporous ceramic heatsink about 30 % lower voltages compared to voltages generated in the WSN node with the aluminum heatsink.

Fig. 10 shows the dependence of the power that TEG transfers to the load as a function of temperature difference for the WSN nodes with different combinations of TEG-heatsink. Following the values of the generated voltage, the value of power also increases with increasing the temperature difference. The choice of the TEG and the heatsink affects the load power value in the same way as the load voltage value. The power value ranges from 0.7 mW for the WSN node with TEG1 and HS3 at the temperature difference of 15 °C up to 66.5 mW for the node with TEG3 and HS2 at the temperature difference of 50 °C.
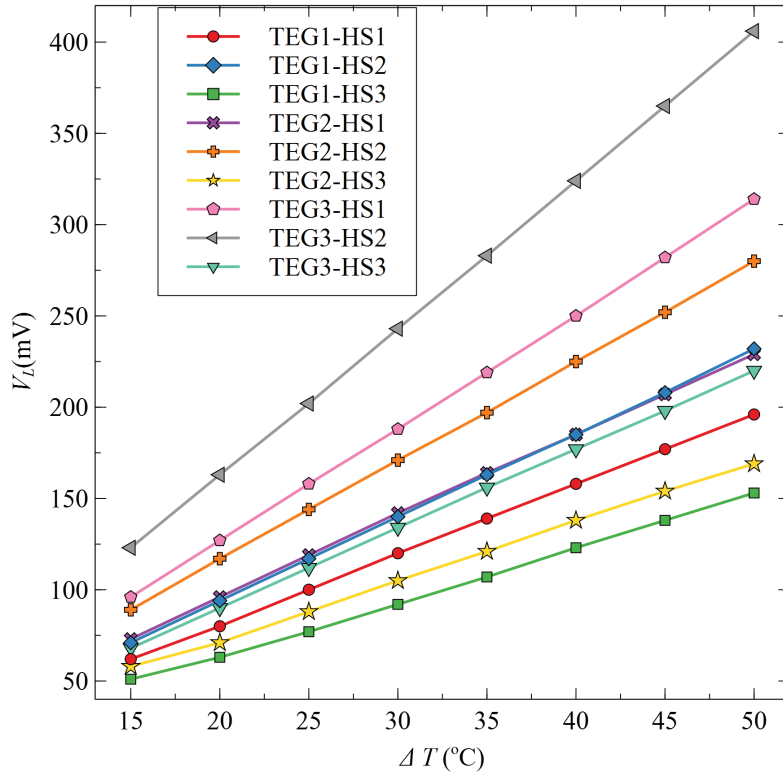
Fig. 9: Generated load voltage vs. temperature difference for WSN nodes with different TEG-heatsink combinations.

The overall system harvesting efficiency is calculated by:

$$\eta = \frac{P_L}{Q_{HEAT}}, \tag{15}$$

where Q_{HEAT} represents heat flux of the heater, i.e., the current through the T_{HEAT} voltage generator in schematics. According to Fig. 10, the increase of the temperature difference causes the overall efficiency increase. Fig. 11 shows the efficiency values for all investigated WSN nodes at a temperature difference of 25 °C and 50 °C. The WSN node with TEG1 and HS3 shows the lowest efficiency (0.09 %), while the WSN node with TEG3 and HS2 heatsink (0.26 %) has the highest efficiency. For all considered TEGs, assemblies with microporous ceramic heatsink show the lowest harvesting efficiency (0.09 % - 0.13 %), which is about 50 % lower efficiency compared to assemblies with alumina heatsink. Alumina heatsinks give the highest efficiency (0.15 % -
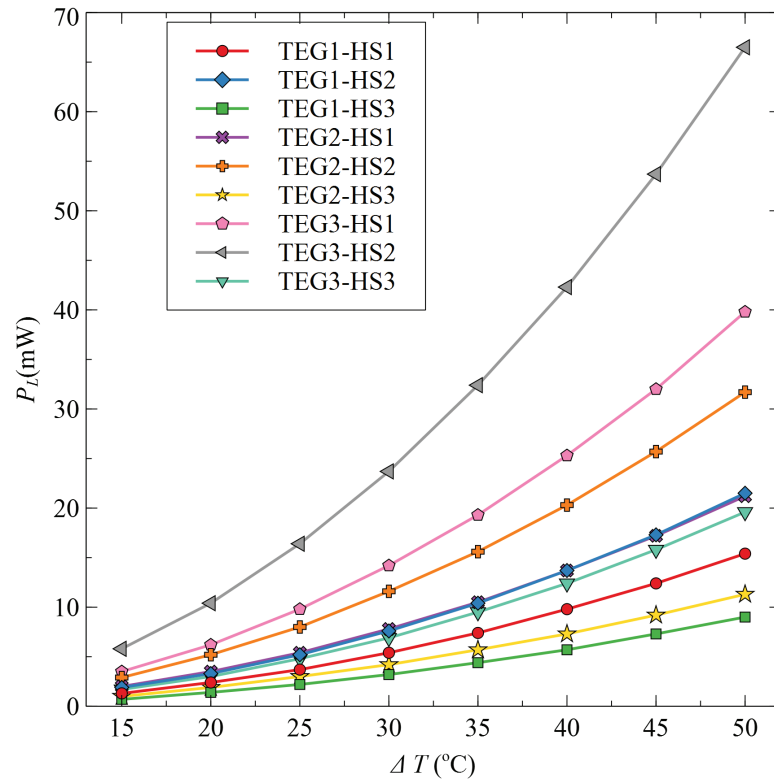
Fig. 10: Generated load power vs. temperature difference for WSN nodes with different TEG-heatsink combinations.

0.26 %), which is about 30 % higher compared to the assemblies with aluminum heatsink (0.12 % - 0.2 %). TEGs with smaller number of thermoelectric pairs require about 25 % higher temperature difference to achieve the same efficiency as larger TEGs. Thus, WSN with TEG1 and HS2 will have an efficiency of 0.26 % at a temperature difference of 50 °C, while the same efficiency will be achieved in a system with TEG3 and HS2 already at a temperature difference of 25 °C. The low overall harvesting efficiency is primarily governed by the low TEG conversion efficiency (1 % -2 %) at small temperature differences present due to the specific temperature distribution through the node elements affected by the natural convection as the worst-case for heat dissipation.

Similar thermoelectric energy harvesting systems have overall efficiency values of the same order. In [43], a wireless sensor node for industrial use provides $0.14\,\mathrm{mW}$ of power at $\Delta T = 7.5\,°\mathrm{C}$. WSN node for indoor
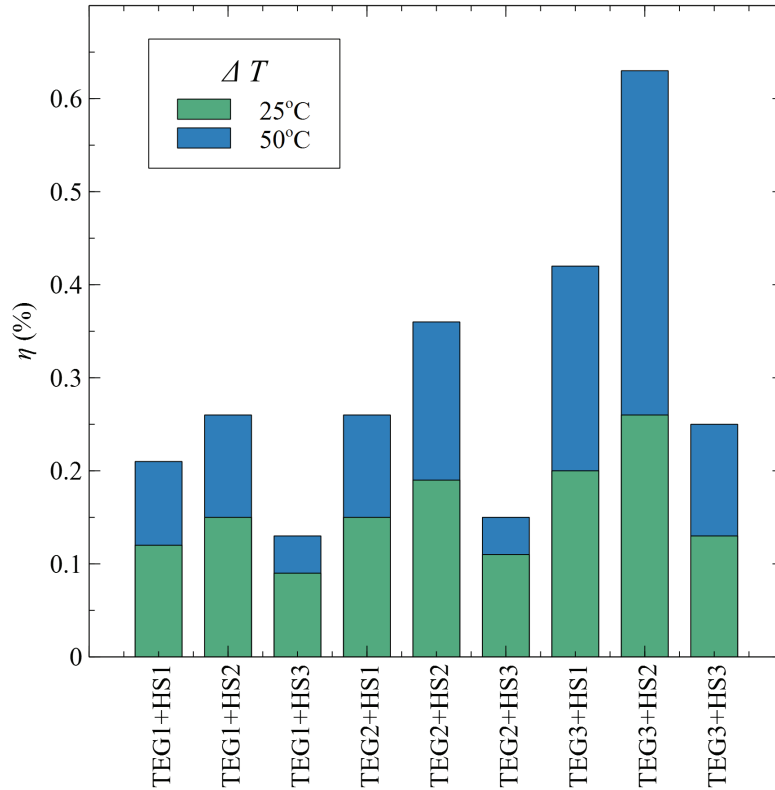
Fig. 11: The overall system harvesting efficiency for WSN nodes with different TEG-heatsink combinations.

use, mountable on hot pipes of installations [44], has an output power of 1.1 mW at $\Delta T = 30\,°C$. The authors of the WSN node for temperature measurement [45] have experimentally shown that 13.1 mW is generated at $\Delta T = 14\,°C$. An accelerometer-based system for a saw blade wear detection [46] is thermoelectrically powered with 1.8 mW at $\Delta T = 30\,°C$. The sensor system with 3 TEGs presented in [47], placed on the user's hand, can generate 1.62 mW of power at $\Delta T = 5\,°C$. The authors in paper [48] presented a prototype of a sensor node containing the TEG made of silicon as thermoelectric material. This node obtains an output power of 34 mW at $\Delta T = 70\,°C$. The distinctive characteristic of the here described WSN node, compared to others available in the literature, is its compact and robust design based on aluminum PCBs and commercially available TEGs and heatsinks.

5   Conclusion

The spatial SPICE compatible models overbridge the incompatibility of multi-physics CAD simulation tools with electrical circuit simulators. Such models enable the simulation of non-electrical and electrical parts simultaneously. This paper presents a spatial SPICE model of a wireless sensor network node made of non - electrical elements (such as aluminum PCBs and heatsink) and a thermoelectric generator. The values of the model parameters are determined from datasheets of the node elements and their materials' technical specifications. Comparison of the experimental and simulation results confirms the validity of the model. The developed model was used to characterize the WSN nodes with different TEGs and heatsinks to define the most suitable combination in terms of energy conversion efficiency. Each considered TEG in combination with an alumina ceramic heatsink gives 30 % higher conversion efficiency than with an aluminum heatsink and about 50 % higher efficiency than in combination with a microporous ceramic heatsink. The miniaturization criterion in the design of the WSN nodes imposes a need for a TEG of smaller overall dimensions. Such TEG, due to the smaller number of thermoelectric pairs, needs about a 25 % higher temperature difference to reach the same conversion efficiency as larger TEGs. The model also enables the simulation of different WSN nodes in the steady-state and time domain to determine the cold start time and the maximum applicable temperature.

Acknowledgments

References

[1] S. Kasap, *Principles of Electronic Materials and Devices*. Paperbackshop UK Import, Apr. 2017.

[2] M. Chen, L. Rosendahl, T. Condra, and J. Pedersen, "Numerical modeling of thermoelectric generators with varing material properties in a circuit simulator," *IEEE Transactions on Energy Conversion*, vol. 24, no. 1, pp. 112–124, mar 2009.

[3] D. Mitrani, J. Tome, J. Salazar, A. Turo, M. Garcia, and J. Chavez, "Methodology for extracting thermoelectric module parameters," *IEEE Transactions on Instrumentation and Measurement*, vol. 54, no. 4, pp. 1548–1552, aug 2005.

[4] S. Dalola, M. Ferrari, V. Ferrari, M. Guizzetti, D. Marioli, and A. Taroni, "Characterization of thermoelectric modules for powering autonomous sensors," *IEEE Transactions on Instrumentation and Measurement*, vol. 58, no. 1, pp. 99–107, jan 2009.

[5] J. García-Cañadas and G. Min, "Low frequency impedance spectroscopy analysis of thermoelectric modules," *Journal of Electronic Materials*, vol. 43, no. 6, pp. 2411–2414, mar 2014.

[6] D. Milić, A. Prijić, Lj. Vračar, and Z. Prijić, "Characterization of commercial thermoelectric modules for application in energy harvesting wireless sensor nodes," *Applied Thermal Engineering*, vol. 121, pp. 74–82, jul 2017.

[7] M. Maaspuro, "Experimenting and simulating thermoelectric cooling of an LED module," *International Journal of Online and Biomedical Engineering (iJOE)*, vol. 11, no. 4, p. 47, aug 2015.

[8] S. A. Afghan and H. Géza, "Modelling and analysis of energy harvesting in internet of things (IoT): Characterization of a thermal energy harvesting circuit for IoT based applications with LTC3108," *Energies*, vol. 12, no. 20, p. 3873, oct 2019.

[9] M. O. Cernaianu and A. Gontean, "High-accuracy thermoelectrical module model for energy-harvesting systems," *IET Circuits, Devices & Systems*, vol. 7, no. 3, pp. 114–123, may 2013.

[10] S. Siouane, S. Jovanović, and P. Poure, "Equivalent electrical circuits of thermoelectric generators under different operating conditions," *Energies*, vol. 10, no. 3, p. 386, mar 2017.

[11] A. Prijić, M. Marjanović, Lj. Vračar, D. Danković, D. Milić, and Z. Prijić, "A steady-state spice modeling of the thermoelectric wireless sensor network node," in *Proceedings of 4th International Conference on Electrical, Electronics and Computing Engineering,IcETRAN 2017*, 2017, pp. MOI2.3.1–6.

[12] F. Felgner, L. Exel, M. Nesarajah, and G. Frey, "Component-oriented modeling of thermoelectric devices for energy system design," *IEEE Transactions on Industrial Electronics*, vol. 61, no. 3, pp. 1301–1310, mar 2014.

[13] A. Prijić, Lj. Vračar, D. Vučković, D. Milić, and Z. Prijić, "Thermal energy harvesting wireless sensor node in aluminum core PCB technology," *IEEE Sensors Journal*, vol. 15, no. 1, pp. 337–345, jan 2015.

[14] Z. Prijić, A. Prijić, and Lj. Vračar, "Design techniques for wireless sensor network nodes powered by ambient energy harvesting," in *2019 IEEE 31st International Conference on Microelectronics (MIEL)*.   IEEE, sep 2019.

[15] M. Marjanović, A. Prijić, B. Randjelović, and Z. Prijić, "A transient modeling of the thermoelectric generators for application in wireless sensor network nodes," *Electronics*, vol. 9, no. 6, p. 1015, jun 2020.

[16] A. Bhattacharyya, "Heat transfer analogies," Aktiebolaget atomenergi, Tech. Rep., 1965.

[17] J. Chavez, J. Ortega, J. Salazar, A. Turo, and M. Garcia, "SPICE model of thermoelectric elements including thermal effects," in *Proceedings of the 17th IEEE Instrumentation and Measurement Technology Conference [Cat. No. 00CH37066]*, vol. 2. IEEE, 2000, pp. 1019–1023.

[18] S. Lineykin and S. Ben-Yaakov, "Analysis of thermoelectric coolers by a spice-compatible equivalent-circuit model," *IEEE Power Electronics Letters*, vol. 3, no. 2, pp. 63–66, jun 2005.

[19] P. Salome, C. Leroux, P. Crevel, and J. P. Chante, "Investigations on the thermal behavior of interconnects under ESD transients using a simplified thermal RC network," *Microelectronics Reliability*, vol. 39, no. 11, pp. 1579–1591, nov 1999.

[20] C. Bekhaled, S. Hlioui, L. Vido, M. Gabsi, M. Lecrivain, and Y. Amara, "3D magnetic equivalent circuit model for homopolar hybrid excitation synchronous machines," in *2007 International Aegean Conference on Electrical Machines and Power Electronics*, sep 2007.

[21] T.-Y. Wang and C. C.-P. Chen, "SPICE-compatible thermal simulation with lumped circuit modeling for thermal reliability analysis based on modeling order reduction," in *SCS 2003. International Symposium on Signals, Circuits and Systems. Proceedings (Cat. No.03EX720)*. IEEE Comput. Soc, 2004, pp. 357–362.

[22] K. Carstens, M. Reuter, J. Cichoszewski, P. Gedeon, and J. Werner, "Influence of thickness deviation on crystalline silicon solar cell performance," *Energy Procedia*, vol. 8, pp. 461–466, 2011.

[23] M. Pedram and S. Nazarian, "Thermal modeling, analysis, and management in vlsi circuits: Principles and methods," *Proceedings of the IEEE*, vol. 94, no. 8, pp. 1487–1501, 2006.

[24] A. Sridhar, A. Vincenzi, D. Atienza, and T. Brunschwiler, "3D-ICE: A compact thermal model for early-stage design of liquid-cooled ics," *IEEE Transactions on Computers*, vol. 63, no. 10, pp. 2576–2589, 2014.

[25] G. Floros, K. Daloukas, N. Evmorfopoulos, and G. Stamoulis, "A preconditioned iterative approach for efficient full chip thermal analysis on massively parallel platforms," *Technologies*, vol. 7, no. 1, p. 1, dec 2018.

[26] S. Lineykin, M. Sitbon, and A. Kuperman, "Spatial equivalent circuit model for simulation of on-chip thermoelectric harvesters," *Micromachines*, vol. 11, no. 6, p. 574, jun 2020.

[27] J. Araque–Mora and L. Angel, "Distributed equivalent circuit for modeling heat transfer process in a thermoelectric system," in *2021 IEEE 5th Colombian Conference on Automatic Control (CCAC)*, 2021, pp. 326–331.

[28] Thermoel toolkit, Seebeck coefficient predictive component. [Online]. Available: http://info.eecs.northwestern.edu/SeebeckCoefficientPredictor

[29] Pubchem. National Center for Biotechnology Information, U.S. National Library of Medicine. [Online]. Available: https://pubchem.ncbi.nlm.nih.gov/

[30] Y. Moumouni and R. Jacob Baker, "Concise thermal to electrical parameters extraction of thermoelectric generator for spice modeling," in *2015 IEEE 58th International Midwest Symposium on Circuits and Systems (MWSCAS)*, 2015, pp. 1–4.

[31] "Linear technology corporation, circuit design tools calculators–LTSpice." [Online]. Available: https://www.analog.com/en/design-center/design-tools-and-calculators/ltspice-simulator.html

[32] "Adaptive, et-031-10-20, peltier cooler module, datasheet." [Online]. Available: https://www.europeanthermodynamics.com/products/datasheets/0-ET-031-10-20.pdf

[33] "Adaptive, et-071-08-15, thermoelectric module, datasheet." [Online]. Available: https://www.europeanthermodynamics.com/products/datasheets/ET-071-08-15.pdf

[34] "Adaptive, gm200-71-14-16, thermoelectric generator module, datasheet." [Online]. Available: https://www.europeanthermodynamics.com/products/datasheets/GM200-71-14-1620(2).pdf

[35] "Custom thermoelectric, material properties." [Online]. Available: https://customthermoelectric.com/tech-info/more-useful-info/material-properties.html

[36] H. Goldsmid, "Bismuth telluride and its alloys as materials for thermoelectric generation," *Materials*, vol. 7, no. 4, pp. 2577–2592, mar 2014.

[37] I. T. Witting, T. C. Chasapis, F. Ricci, M. Peters, N. A. Heinz, G. Hautier, and G. J. Snyder, "The thermoelectric properties of bismuth telluride," *Advanced Electronic Materials*, vol. 5, no. 6, p. 1800904, apr 2019.

[38] "Ceramic heat spreader pin fin series, datasheet." [Online]. Available: https://www.farnell.com/datasheets/2012338.pdf

[39] "Ceramic heat sinks for cooling of leds and semiconductors drivers, article." [Online]. Available: http://endrich.hu/

[40] "Amec thermasol, ceramic heatsink introduction, slides." [Online]. Available: https://amecthermasol.co.uk/

[41] M. Marjanović, A. Stojković, A. Prijić, D. Danković, and Z. Prijić, "A SPICE compatible spatial equivalent circuit model of the heatsink," in *2021 IEEE 32nd International Conference on Microelectronics (MIEL)*. IEEE, sep 2021.

[42] "Linear technology corporation, LTC3108 ultralow voltage step-up converter and power manager, datasheet." [Online]. Available: https://www.analog.com/media/en/technical-documentation/datasheets/LTC3108.pdf

[43] J. M. Lopera, H. del Arco Rodriguez, J. M. P. Pereira, A. R. de Castro, and J. L. R. Vigil, "Practical issues in the design of wireless sensors supplied by energy harvesting thermoelectric generators," *IEEE Transactions on Industry Applications*, vol. 55, no. 1, pp. 996–1005, jan 2019.

[44] W. Wang, V. Cionca, N. Wang, M. Hayes, B. O'Flynn, and C. O'Mathuna, "Thermoelectric energy harvesting for building energy management wireless sensor networks," *International Journal of Distributed Sensor Networks*, vol. 9, no. 6, p. 232438, jun 2013.

[45] L. Hou, S. Tan, Z. Zhang, and N. W. Bergmann, "Thermal energy harvesting WSNs node for temperature monitoring in IIoT," *IEEE Access*, vol. 6, pp. 35 243–35 249, 2018.

[46] M. Magno, L. Sigrist, A. Gomez, L. Cavigelli, A. Libri, E. Popovici, and L. Benini, "SmarTEG: An autonomous wireless sensor node for high accuracy accelerometer-based monitoring," *Sensors*, vol. 19, no. 12, p. 2747, jun 2019.

[47] C. Xia, D. Zhang, W. Pedrycz, K. Fan, and Y. Guo, "Human body heat based thermoelectric harvester with ultra-low input power management system for wireless sensors powering," *Energies*, vol. 12, no. 20, p. 3942, oct 2019.

[48] J.-P. Im, J. Kim, J. Lee, J. Woo, S. Im, Y. Kim, Y.-S. Eom, W. Choi, J. Kim, and S. Moon, "Self-powered autonomous wireless sensor node by using silicon-based 3D thermoelectric energy generator for environmental monitoring application," *Energies*, vol. 13, no. 3, p. 674, feb 2020.